Nonlinear thermal responses in geometrically anisotropic metamaterials

Pengfei Zhuang,[1] Jun Wang,[2,3,*] Shuai Yang,[1] and Jiping Huang[1,†]
[1]*Department of Physics, State Key Laboratory of Surface Physics, and Key Laboratory of Micro and Nano Photonic Structures (MOE), Fudan University, Shanghai 200433, China*
[2]*School of Physics, East China University of Science and Technology, Shanghai 200237, China*
[3]*Wenzhou Institute, University of Chinese Academy of Sciences, Wenzhou 325001, China*

(Received 18 July 2022; accepted 22 September 2022; published 11 October 2022)

Nonlinear metamaterials have great potential in heat management, which has aroused intensive research interest in both theory and application, especially for their response to surroundings. However, most existing works focus on geometrically isotropic (circular) structures, limiting the potential versatile functionalities. On the other hand, anisotropy in architecture promisingly offers an additional degree of freedom in modulating directional heat transfer. Here, we investigate nonlinear composition effects in geometrically anisotropic (confocal elliptical) thermal medium under the framework of effective medium approximation, and deduce a series of general formulas for quantitatively predicting nonlinearity enhancement. Enhancement coefficients are analytically derived by the Taylor expansion method in different nonlinearity cases. In particular, we find that some coupling conditions can greatly promote the nonlinear modulation coefficients, introducing stronger enhancement beyond isotropic construction. Our theoretical predictions are verified by finite-element simulation, and feasible experimental suggestions are also given. For extending these results to practical scenes, two intelligent thermal metadevices are designed in proof of concept and demonstrated by numerical simulation. Our works provide a unified theory for anisotropic nonlinear thermal metamaterial design and may benefit flexible applications in self-adaptive thermal management, such as switchable cloaks, concentrators, or macroscopic thermal diodes.

DOI: 10.1103/PhysRevE.106.044203

I. INTRODUCTION

With the rapid development of artificial structure design for manipulating and managing heat flow [1–8], various thermal metamaterials with advanced functionalities beyond natural-occurring materials have been achieved, such as thermal cloaks [9–14], thermal concentrators [15–20], thermal rotators [21,22], thermal camouflage [23], thermal illusion [24], etc. However, most existing research does not take the nonlinear effect into account, that is, intrinsic parameters of constitutive materials are temperature dependent [25,26]. The actual physical existence is usually nonlinear or stimulus responsive, for example, the response of polarization to external electric fields (nonlinear optics [27,28]). In analogy with nonlinear optical response, thermal conductivities of materials are practically dependent on ambient temperature to some extent (nonlinear thermotics [29]), which may introduce challenges in theoretical mechanism but opportunities for developing intelligent thermal metamaterials.

Fortunately, nonlinear transformation thermotics [30] has been proposed for treating temperature-dependent constitutive materials and inspired switchable thermal metadevices [31–35]. More recently, nonlinear thermotics has been extended to solving thermal wave-related regulation issues [36–39] and nonlinear thermal conductivities of composite structures [40–43], indicating that nonlinearity in artificial thermal systems contains fantastic physics and promising application prospect. In particular, the core-shell structure, a typical scheme, exhibits glorious abilities to regulate heat flow in different directions with geometric anisotropy [44,45]. It is determinate that combining anisotropic configurations and nonlinearity may lead to theoretical difficulties in structure design but serve for advanced multiple degrees of control freedom in thermal regulation.

In this work, we investigate the nonlinearity enhancement of confocal elliptical core-shell structures with temperature-dependent thermal conductivities, which means that the response of effective nonlinear thermal conductivity to temperature will be enhanced [41]. The enhancement effect of composite induced by core, shell, and background are studied, respectively. Then, we focus on a group of specific coupling conditions [46–48], where the properties of the core can be extended to the entire composite. In other words, the effective thermal conductivity [31,35] of the shell will be the same as that of the core. By applying the Taylor formula, we expand the effective thermal conductivity of the composite (in the case of two and three dimensions) to a finite order and define the nonlinear modulation coefficient. These theoretical results are verified by finite-element simulation. The thermal coupling conditions require apparent negative

*wj21@ecust.edu.cn
†jphuang@fudan.edu.cn

conductivity [49,50], which can be effectively realized with external heat energy. Finally, as a practical application, we design two types of intelligent metamaterials, which can automatically switch different functions according to external temperature and heat flux direction. These results may have potential application in novel thermal encoding [51] and nonreciprocity [52] and provide guidance to other diffusive systems, such as plasma transport [53], for achieving similar behaviors.

II. THEORY

A. General theory for two-dimensional nonlinear enhancement

First of all, we consider a confocal core-shell ellipse structure embedded in a finite background. The semimajor and semiminor axis lengths of core (or shell) are denoted as r_{c1} and r_{c2} (or r_{s1} and r_{s2}), respectively. For materials with linear thermal conductivities, the effective thermal conductivity of core-shell structure can be calculated based on the effective medium approximation as [54]

$$\kappa_{csi} = \kappa_s \frac{L_{ci}\kappa_c + (1-L_{ci})\kappa_s + f_1(1-L_{si})(\kappa_c-\kappa_s)}{L_{ci}\kappa_c + (1-L_{ci})\kappa_s - f_1 L_{si}(\kappa_c-\kappa_s)}, \quad (1)$$

and that of core-shell structure plus background can be expressed as [58]

$$\kappa_{ei} = k_b \frac{L_{si}\kappa_{csi} + (1-L_{si})\kappa_b + f_2(1-L_{si})(\kappa_{csi}-\kappa_b)}{L_{si}\kappa_{csi} + (1-L_{si})\kappa_b - f_2 L_{si}(\kappa_{csi}-\kappa_b)}, \quad (2)$$

where the inner and outer area fraction can be expressed as $f_1 = r_{c1}r_{c2}/(r_{s1}r_{s2})$ and $f_2 = \pi r_{s1}r_{s2}/S_0$, and S_0 is the total area of background plus core and shell. L_{w1} (or L_{w2}) is the shape factor along the direction of semimajor (or semiminor) axis, which can be defined as $L_{w1} = r_{w2}/(r_{w1}+r_{w2})$ [or $L_{w2} = r_{w1}/(r_{w1}+r_{w2})$], where the subscript w can take c or s for core or shell. It is worth mentioning that the shape factors satisfy $L_{w1} + L_{w2} = 1$. Its degree of deviation from 0.5 means the flattening of an ellipse.

Then, we introduce the temperature-dependent thermal conductivity of actual material, which usually shows a power-law relationship between parameter and temperature. For the sake of convenience and without loss of generality, we consider three cases shown in Fig. 1, where one part of the ternary structure has a stronger nonlinear thermal conductivity than the others. Therefore, we regard the weaker nonlinear thermal conductivities as temperature independent and express the stronger nonlinear thermal conductivity as

$$\tilde{\kappa}_c(T) = \kappa_c + \chi_c T^\alpha, \quad (3a)$$

$$\tilde{\kappa}_s(T) = \kappa_s + \chi_s T^\alpha, \quad (3b)$$

$$\tilde{\kappa}_b(T) = \kappa_b + \chi_b T^\alpha. \quad (3c)$$

Here, χ_c, χ_s, and χ_b are the nonlinear coefficients and α can be any real number. It is noted that if we analogy the dependence of the polarizability on the electric field intensity or its higher-order terms described in nonlinear optics [28,55,56], the thermal conductivity in nonlinear thermotics should be responsive to the temperature gradient. Nevertheless, thermal conductivities of natural materials are basically dependent on temperature [57], generally depicted by Eqs. (3a)–(3c).

As we consider a common case that thermal conductivity is weakly temperature-dependent, i.e., $\chi_c T^\alpha \ll \kappa_c$, $\chi_s T^\alpha \ll \kappa_s$, or $\chi_b T^\alpha \ll \kappa_b$, we can substitute Eqs. (3a)–(3c) into Eqs. (1) and (2) separately. Then, we expand temperature-dependent effective thermal conductivities of these three schemes up to T^α term by Taylor's formula as

$$\tilde{\kappa}_{ei}^{(c)}(T) = \kappa_{ei} + \chi_{ei}^{(c)} T^\alpha + O(T^\alpha), \quad (4a)$$

$$\tilde{\kappa}_{ei}^{(s)}(T) = \kappa_{ei} + \chi_{ei}^{(s)} T^\alpha + O(T^\alpha), \quad (4b)$$

$$\tilde{\kappa}_{ei}^{(b)}(T) = \kappa_{ei} + \chi_{ei}^{(b)} T^\alpha + O(T^\alpha), \quad (4c)$$

where $\chi_{ei}^{(c)}$, $\chi_{ei}^{(s)}$, and $\chi_{ei}^{(b)}$ are

$$\chi_{ei}^{(c)} = \lambda_{i1}\chi_c, \quad (5a)$$

$$\chi_{ei}^{(s)} = \lambda_{i2}\chi_s, \quad (5b)$$

$$\chi_{ei}^{(b)} = \lambda_{i3}\chi_b. \quad (5c)$$

λ is related to geometric parameters (f_1, f_2, L_{ci}, and L_{si}) and linear thermal conductivities (κ_c, κ_s, and κ_b), which will be presented hereafter.

Equations (4a)–(4c) reveal the power dependence of effective thermal conductivities of the ternary structures on temperature. In addition, the response of conductivity to temperature is weak, so we can neglect the high-order nonlinear term [$O(T^\alpha)$] compared with the first-order term (T^α). Then, we can define the nonlinear modulation coefficients for nonlinear core $\eta_i^{(c)} = \chi_{ei}^{(c)}/\chi_c$, nonlinear shell $\eta_i^{(s)} = \chi_{ei}^{(s)}/\chi_c$, and nonlinear background $\eta_i^{(b)} = \chi_{ei}^{(b)}/\chi_b$ respectively, which are given by

$$\eta_i^{(c)} = \lambda_{i1}, \quad (6a)$$

$$\eta_i^{(s)} = \lambda_{i2}, \quad (6b)$$

$$\eta_i^{(b)} = \lambda_{i3}, \quad (6c)$$

To explore the nonlinear enhancement effect ($\eta > 1$), we draw the nonlinear modulation coefficients as functions of geometric parameters with constant κ_s/κ_c and κ_b/κ_c. Nevertheless, these geometric parameters (f_1, f_2, L_{ci}, and L_{si}) are not independent of each other and cannot visually reflect the contribution of each region (core, shell, and background). Thus, we aim to express η by two independent geometric parameters L_{c1} and L_{s1}. According to the definition of confocal ellipse and shape factors, we have

$$r_{c1}^2 - r_{c2}^2 = r_{s1}^2 - r_{s2}^2 = c^2, \quad (7a)$$

$$L_{c1} = \frac{r_{c2}}{r_{c1}+r_{c2}}, \quad (7b)$$

$$L_{s1} = \frac{r_{s2}}{r_{s1}+r_{s2}}, \quad (7c)$$

where the core-shell structure is confocal and c is the half focal length. Then, we can derive

$$r_{w1} = \sqrt{\frac{c^2}{1-2L_{w1}}}(1-L_{w1}), \quad (8a)$$

$$r_{w2} = \sqrt{\frac{c^2}{1-2L_{w1}}}L_{w1}, \quad (8b)$$

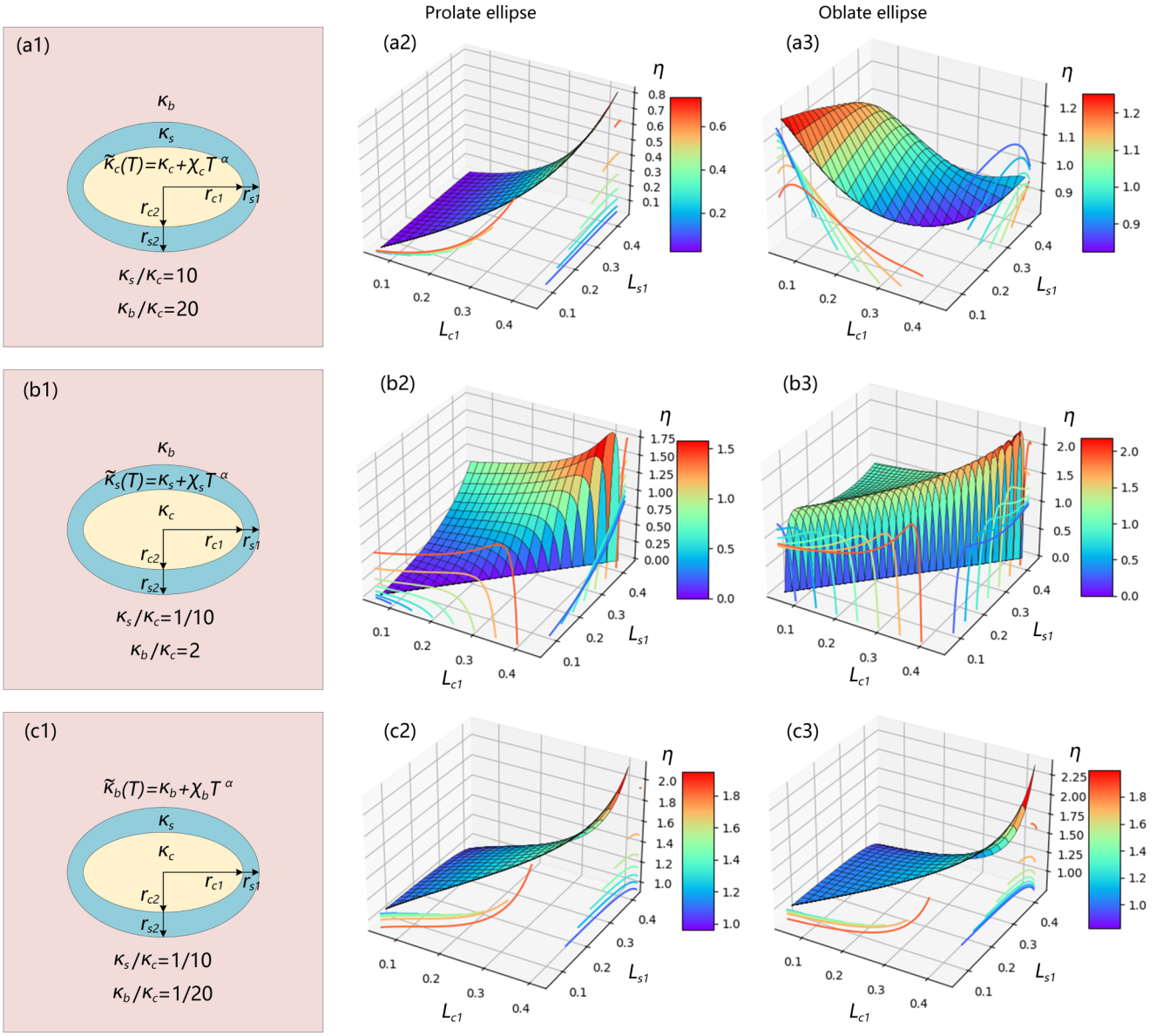

FIG. 1. Two-dimensional schematic diagram of the composite structure with (a1) nonlinear core, (b1) nonlinear shell, or (c1) nonlinear background. (a2), (a3) [(b2), (b3) or (c2), (c3)] The nonlinear modulation coefficient η of (a1) [(b1) or (c1)] as a function of configuration L_{c1} and L_{s1}. (a2), (b2), (c2) With prolate ellipse. (a3), (b3), (c3) With oblate ellipse. (a2)–(c3) The color lines in the left (or right) side show η as a function of L_{c1} (or L_{s1}) with constant L_{s1} (or L_{c1}). Parameters: (a1)–(a3) $\kappa_s/\kappa_c = 10$ and $\kappa_b/\kappa_c = 20$; (b1)–(b3) $\kappa_s/\kappa_c = 1/10$ and $\kappa_b/\kappa_c = 2$; (c1)–(c3) $\kappa_s/\kappa_c = 1/10$ and $\kappa_b/\kappa_c = 1/20$; and $c^2 = 4.69$, $\chi_c = \chi_s = \chi_b = 0.001$, $\alpha = 1$, and background size 8×6 cm^2 for (a1)–(c3).

$$f_1 = \frac{(1-2L_{s1})(1-L_{c1})L_{c1}}{(1-2L_{c1})(1-L_{s1})L_{s1}}, \tag{8c}$$

$$f_2 = \frac{\pi c^2(1-L_{s1})L_{s1}}{(1-2L_{s1})S_0}. \tag{8d}$$

Thus, we can determine the geometric parameters of three schemes by dimensionless parameters, i.e., L_{c1} and L_{s1}. Figure 1 visually shows the modulation coefficient η as a function of L_{c1} and L_{s1} when c and S_0 are fixed. The prolate and oblate confocal ellipse structures are applied in Figs. 1(a2)–1(c2) and 1(a3)–1(c3), respectively. It is clear that η can exceed 1 under certain thermal conductivity and geometry of the composite. In other words, the nonlinear item can be enhanced by mixing different materials.

Since Eq. (6) is too complicated in detailed form, we mainly use Fig. 1 to predict the value of η. In addition, we can choose certain conditions to simplify Eq. (6), i.e., coupling conditions. Furthermore, the conditions can help us compare the overall nonlinear enhancement more fairly. The effective thermal conductivity of core-shell structure is equal to that of the core and background when the coupling condition of thermal conductivity is satisfied, namely,

$$\kappa_c = \kappa_b, \tag{9a}$$

$$\kappa_c = -\frac{1-L_{ci}-(1-L_{si})f}{L_{ci}-L_{si}f}\kappa_s. \tag{9b}$$

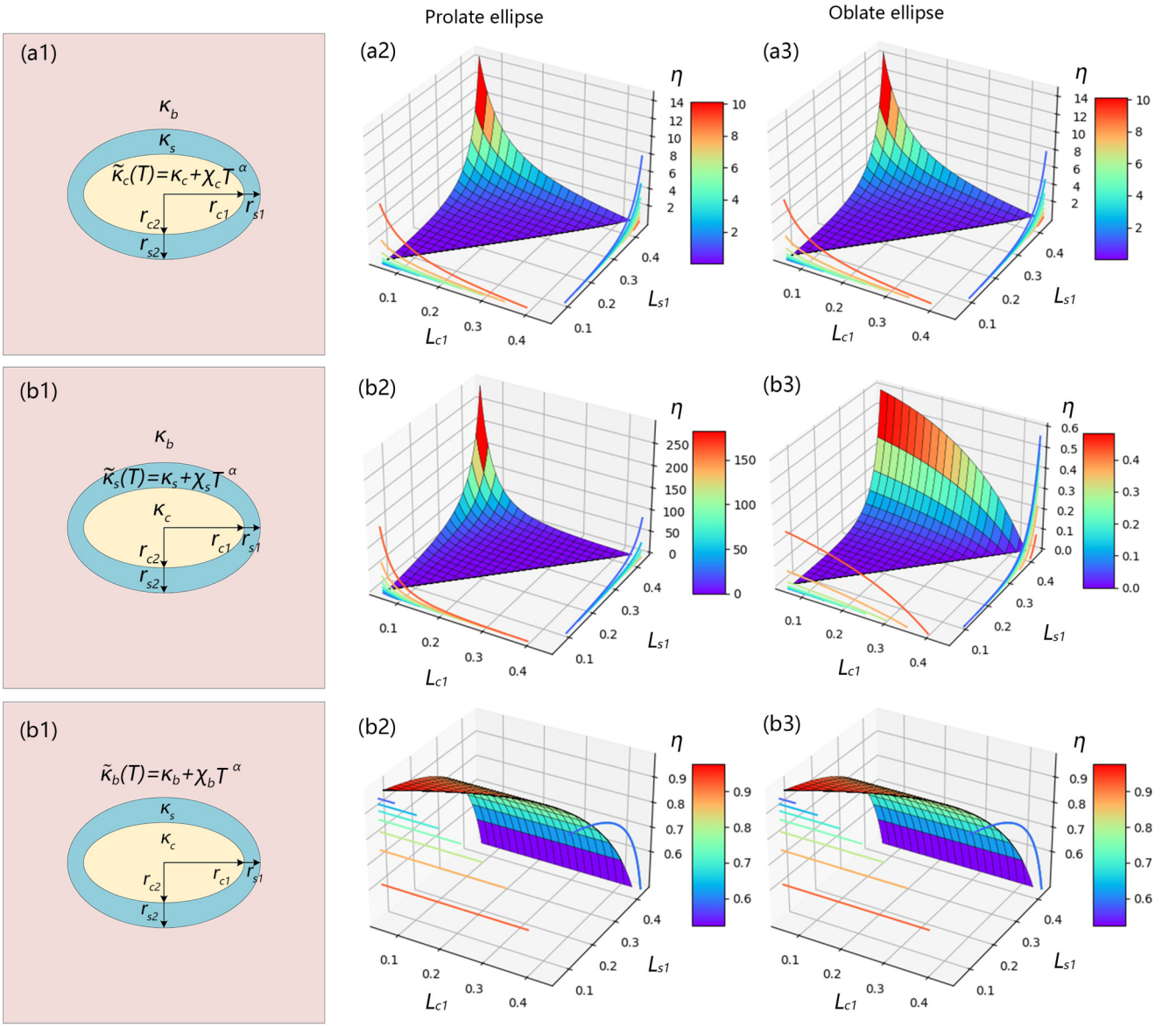

FIG. 2. Two-dimensional schematic diagram of the composite structure with (a1) nonlinear core, (b1) nonlinear shell, or (c1) nonlinear background under the coupling condition. (a2), (a3) [(b2), (b3) or (c2), (c3)] The nonlinear modulation coefficient η of (a1) [(b1) or (c1)] as a function of configuration L_{c1} and L_{s1}. (a2), (b2), (c2) With prolate ellipse. (a3), (b3), (c3) With oblate ellipse. (a2)–(c3) The color lines in the left (or right) side show η as a function of L_{c1} (or L_{s1}) with constant L_{s1} (or L_{c1}). Parameters: $c^2 = 4.69$, and background size 8×6 cm^2 for (a1)–(c3).

If we apply the coupling conditions, the nonlinear modulation coefficient can be rewritten as

$$\eta_i^{(c)} = \frac{\pi c^2(1-L_{s1})^2(1-2L_{c1})L_{s1}^2}{(1-2L_{s1})^2(1-L_{c1})L_{c1}S_0}, \tag{10a}$$

$$\eta_1^{(s)} = \frac{\pi c^2(1-L_{s1})^2(L_{s1}-L_{c1})(1-L_{c1}-L_{s1}+2L_{c1}L_{s1})}{(1-2L_{s1})^2L_{c1}^2S_0}, \tag{10b}$$

$$\eta_2^{(s)} = \frac{\pi c^2L_{s1}^2(L_{s1}-L_{c1})(1-L_{c1}-L_{s1}+2L_{c1}L_{s1})}{(1-2L_{s1})^2(1-L_{c1})^2S_0}, \tag{10c}$$

$$\eta_i^{(b)} = 1-\frac{\pi c^2(1-L_{s1})L_{s1}}{(1-2L_{s1})S_0}, \tag{10d}$$

which shows the direct relationship between η and geometric parameters.

So far, we have deduced η by four independent parameters c^2, L_{c1}, L_{s1}, and S_0. Figure 2 visually indicate the modulation coefficient η as a function of L_{c1} and L_{s1} when c and S_0 are fixed. The prolate (or oblate) confocal ellipse structure is applied in Figs. 2(a2)–2(c2) [or Figs. 2(a3)–2(c3)], where the left side (or the right side) displays η as a function of L_{c1} (or L_{s1}) when L_{s1} (or L_{c1}) takes different values. Apparently, the nonlinear modulation coefficients can be increased by an order of magnitude under the coupling conditions. It is worth mentioning that the conclusions of two-dimensional case can also be extended to three dimensions, which are discussed below.

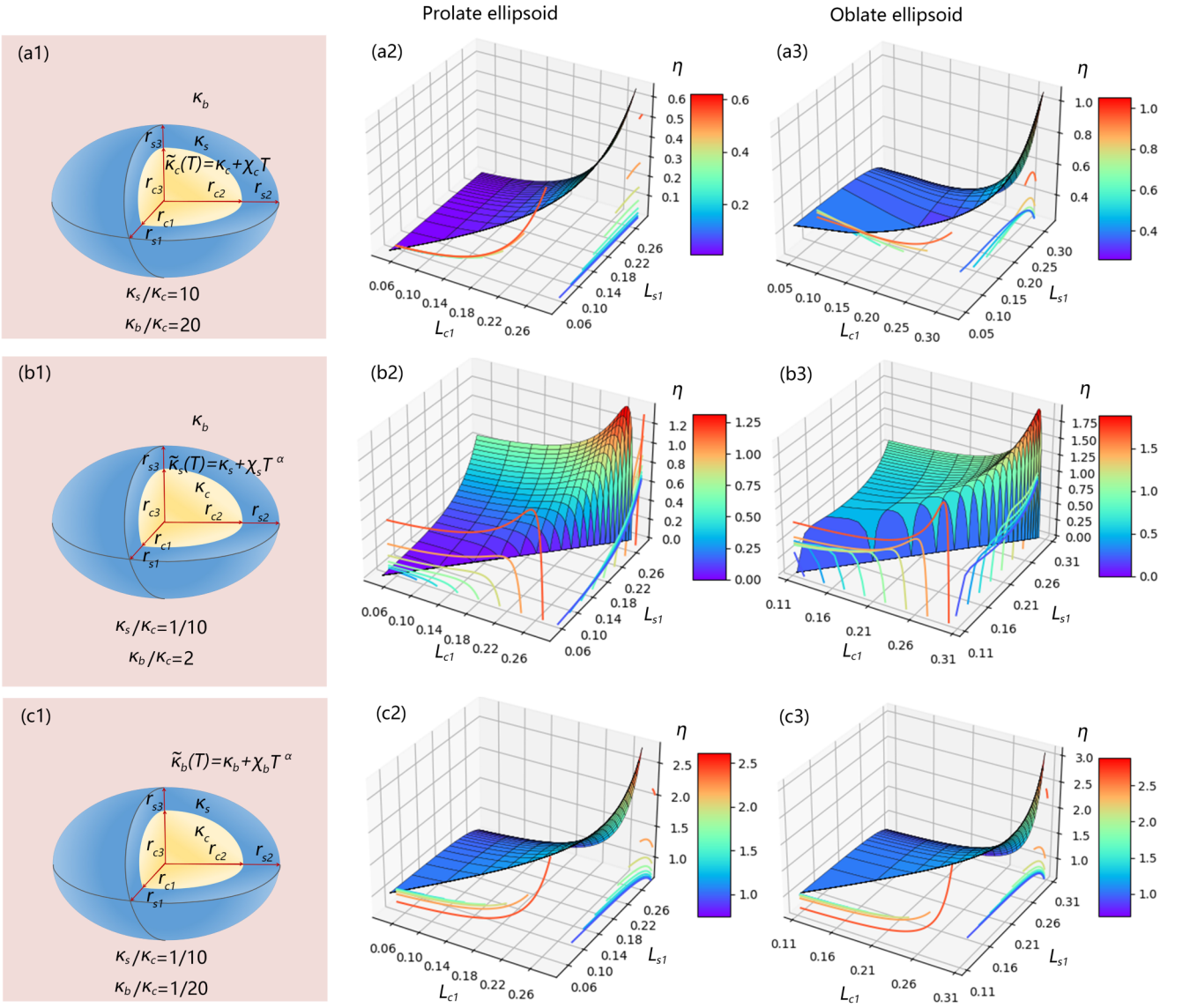

FIG. 3. Three-dimensional schematic diagram of the composite structure with (a1) nonlinear core, (b1) nonlinear shell, or (c1) nonlinear background. (a2), (a3) [(b2), (b3) or (c2), (c3)] The nonlinear modulation coefficient η of (a1) [(b1) or (c1)] as a function of configuration L_{c1} and L_{s1}. (a2), (b2), (c2) With prolate ellipsoid. (a3), (b3), (c3) With oblate ellipsoid. (a2)–(c3) The color lines in the left (or right) side show η as a function of L_{c1} (or L_{s1}) with constant L_{s1} (or L_{c1}). Parameters: (a1)–(a3) $\kappa_s/\kappa_c = 10$ and $\kappa_b/\kappa_c = 20$; (b1)–(b3) $\kappa_s/\kappa_c = 1/10$ and $\kappa_b/\kappa_c = 2$; (c1)–(c3) $\kappa_s/\kappa_c = 1/10$ and $\kappa_b/\kappa_c = 1/20$; and $c^2 = 4.69$, $\chi_c = \chi_s = \chi_b = 0.001$, $\alpha = 1$, and background size $8\times6\times6$ cm^3 for (a1)–(c3).

B. General theory for three-dimensional nonlinear enhancement

We extend the conclusions of confocal ellipse structure from two-dimensional to three-dimensional case. We consider a confocal rotational ellipsoid structure embedded in a finite background [Fig. 3], where $r_{w1} \geqslant r_{w2} = r_{w3}$ for prolate ellipsoids and $r_{w1} = r_{w3} \geqslant r_{w2}$ for oblate spheroids. The subscript w can take c or s, representing the core or shell. The forms of effective thermal conductivities for core-shell structure [54] and core-shell structure plus background [58] are still applicable, which are, respectively, represented as

$$\kappa_{csi} = \kappa_s \frac{L_{ci}\kappa_c + (1-L_{ci})\kappa_s + f_1(1-L_{si})(\kappa_c-\kappa_s)}{L_{ci}\kappa_c + (1-L_{ci})\kappa_s - f_1 L_{si}(\kappa_c-\kappa_s)}. \quad (11)$$

$$\kappa_{ei} = k_b \frac{L_{si}\kappa_{csi} + (1-L_{si})\kappa_b + f_2(1-L_{si})(\kappa_{csi}-\kappa_b)}{L_{si}\kappa_{csi} + (1-L_{si})\kappa_b - f_2 L_{si}(\kappa_{csi}-\kappa_b)}, \quad (12)$$

where volume fraction $f_1 = r_{c1}r_{c2}r_{c3}/(r_{s1}r_{s2}r_{s3})$, $f_2 = 4\pi r_{s1}r_{s2}r_{s3}/3V_0$, and V_0 is the volume of background plus core and shell. The shape factor L_{wi} is generally defined as

$$L_{wi} = \prod_j r_{wj} \int_{\rho_w}^{\infty} (\rho_1 + r_{ci}^2)^{-1} \prod_k (\rho_1 + r_{ck})^{-\frac{1}{2}} d\rho_1/2, \quad (13)$$

For prolate ellipsoids, the expressions of shape factors are reduced to

$$L_{w1} = \frac{1-\epsilon^2}{\epsilon^2}\left\{\frac{1}{2\epsilon}\ln\left(\frac{1+\epsilon}{1-\epsilon}\right) - 1\right\}, \quad (14a)$$

$$L_{w2} = L_{w3} = (1 - L_{w1})/2 \quad (14b)$$

where $\epsilon = \sqrt{1-(r_{w2}/r_{w1})^2}$. While for oblate ellipsoids, they are reduced to

$$L_{w2} = 1 - 2L_{w1} = \frac{1}{\epsilon^2}\left\{1 - \frac{\sqrt{1-\epsilon^2}}{\epsilon}\arcsin\epsilon\right\}, \quad (15a)$$

$$L_{w1} = L_{w3} = (1 - L_{w2})/2. \quad (15b)$$

Moreover, if we take $r_{w3} \to \infty$, the shape factors can be reduced to handle the cylindrical (two-dimensional) case, that is, $L_{w1} = r_{w2}/(r_{w1} + r_{w2})$ and $L_{w2} = r_{w1}/(r_{w1} + r_{w2})$. When one of the ternary components is temperature dependent, namely,

$$\tilde{\kappa}_c(T) = \kappa_c + \chi_c T^\alpha, \quad (16a)$$

$$\tilde{\kappa}_s(T) = \kappa_s + \chi_s T^\alpha, \quad (16b)$$

$$\tilde{\kappa}_b(T) = \kappa_b + \chi_b T^\alpha, \quad (16c)$$

we can expand temperature-dependent effective thermal conductivities of three schemes up to T^α term by Taylor's formula,

$$\eta_i^{(c)} = \lambda_{i1} = \frac{f_1 f_2 k_b^2 k_s^2}{(\phi_{i1} + \phi_{i2})^2}, \quad (17a)$$

$$\eta_i^{(s)} = \lambda_{i2} = \frac{f_2 k_b^2 (\phi_{i3} + \phi_{i4})}{(\phi_{i1} + \phi_{i2})^2}, \quad (17b)$$

$$\eta_i^{(b)} = \lambda_{i3} = \frac{\phi_{i5}(\phi_{i6} + \phi_{i7}) + (\phi_{i8} + \phi_{i9} + \phi_{i10})(\phi_{i11} + \phi_{i12} + \phi_{i13} + \phi_{i14})}{(\phi_{i1} + \phi_{i2})^2}. \quad (17c)$$

The parameters $\phi_{i1} - \phi_{i14}$ are related to thermal conductivities (i.e., κ_c, κ_s, and κ_b), area fractions (i.e., f_1 and f_2), and shape factors (i.e., L_{ci} and L_{si}), which are shown in what follows as

$$\phi_{i1} = (1-f_2)L_{si}k_s[L_{ci}\kappa_c + (1-L_{ci})\kappa_s + f_1(1-L_{si})(\kappa_c - \kappa_s)], \quad (18a)$$

$$\phi_{i2} = [f_2 + (1-f_2)(1-L_{si})]k_b[L_{ci}\kappa_c + (1-L_{ci})\kappa_s - f_1 L_{si}(\kappa_c - \kappa_s)], \quad (18b)$$

$$\phi_{i3} = -f_1\kappa_c\kappa_s, \quad (18c)$$

$$\phi_{i4} = [L_{ci}\kappa_c + (1-L_{ci})\kappa_s + f_1(1-L_{si})(\kappa_c - \kappa_s)][L_{ci}\kappa_c + (1-L_{ci})\kappa_s - f_1 L_{si}(\kappa_c - \kappa_s)], \quad (18d)$$

$$\phi_{i5} = -[1 + L_{si}(-1+f_2)]\kappa_b((L_{ci} - L_{si}f_1)(\kappa_c - \kappa_s) + \kappa_s), \quad (18e)$$

$$\phi_{i6} = (1-L_{si})(1-f_2)\kappa_b[(L_{ci} - L_{si}f_1)(\kappa_c - \kappa_s) + \kappa_s], \quad (18f)$$

$$\phi_{i7} = [L_{si}(-1+f_2) - f_2]\kappa_s[(L_{ci} + f_1 - L_{si}f_1) + \kappa_s], \quad (18g)$$

$$\phi_{i8} = \kappa_b\kappa_s + L_{si}(-1+f_2)(\kappa_b - \kappa_s)\kappa_s, \quad (18h)$$

$$\phi_{i9} = L_{si}^2 f_1(-1+f_2)(\kappa_b - \kappa_s)(\kappa_s - \kappa_c) - L_{si}f_1(\kappa_c - \kappa_s)[\kappa_b + (-1+f_2)\kappa_s], \quad (18i)$$

$$\phi_{i10} = L_{ci}(\kappa_c - \kappa_s)[\kappa_b + L_{si}(-1+f_2)\kappa_b - L_{si}(-1+f_2)\kappa_s], \quad (18j)$$

$$\phi_{i11} = -2(-1+L_{si})L_{si}f_1(-1+f_2)\kappa_b\kappa_c, \quad (18k)$$

$$\phi_{i12} = \kappa_s(-1+L_{si})[2(1+L_{si}f_1)(-1+f_2)\kappa_b + f1(-L_{si} + (-1+L_{si})f_2)\kappa_c], \quad (18l)$$

$$\phi_{i13} = -[1 + (-1+L_{si})f_1][L_{si}(-1+f_2) - f_2]\kappa_s^2, \quad (18m)$$

$$\phi_{i14} = L_{ci}(\kappa_c - \kappa_s)[2(-1+L_{si})(-1+f_2)\kappa_b + (L_{si} + f_2 - L_{si}f_2)\kappa_s]. \quad (18n)$$

It is noticed that f_1, f_2 are area fractions and shape factors $L_{w1} = r_{w2}/(r_{w1} + r_{w2})$ [or $L_{w2} = r_{w1}/(r_{w1} + r_{w2})$] in the two-dimensional case. As far as rotating prolate and oblate ellipsoids are concerned, the relationships between shape factors L_{wi} and semiaxis lengths r_{wi} are defined by Eqs. (14) and (15), which are too complex to do reparameterization for three-dimensional structure. However, the nonlinear modulation coefficients are still indirectly dependent on shape factors. Figure 3 visually shows the modulation coefficient η as a function of L_{c1} and L_{s1} when c and S_0 are fixed. The prolate and oblate confocal ellipsoid structures are applied in Figs. 3(a2)–3(c2) and 3(a3)–3(c3), respectively.

Similarly, we introduce the coupling conditions for the three-dimensional case as

$$\kappa_c = \kappa_b, \quad (19a)$$

$$\kappa_c = -\frac{1 - L_{ci} - (1-L_{si})f}{L_{ci} - L_{si}f}\kappa_s. \quad (19b)$$

then Eq. (17) can be reduced to

$$\eta_i^{(c)} = \frac{f_2}{f_1}, \quad (20a)$$

$$\eta_i^{(s)} = \frac{f_2(f_1 - 1)[(1-L_{si})f_1 - (1-L_{ci})]}{f_1(L_{ci} - L_{si}f_1)}, \quad (20b)$$

$$\eta_i^{(b)} = 1 - f_2. \quad (20c)$$

Figure 4 visually shows the modulation coefficient η as a function of L_{c1} and L_{s1} when c and S_0 are fixed. The prolate (or oblate) confocal ellipsoid structure is applied in Figs. 4(a2)–4(c2) [or Figs. 4(a3)–4(c3)], where the left side (or the right side) displays η as a function of L_{c1} (or L_{s1}) when L_{s1} (or L_{c1}) take different values.

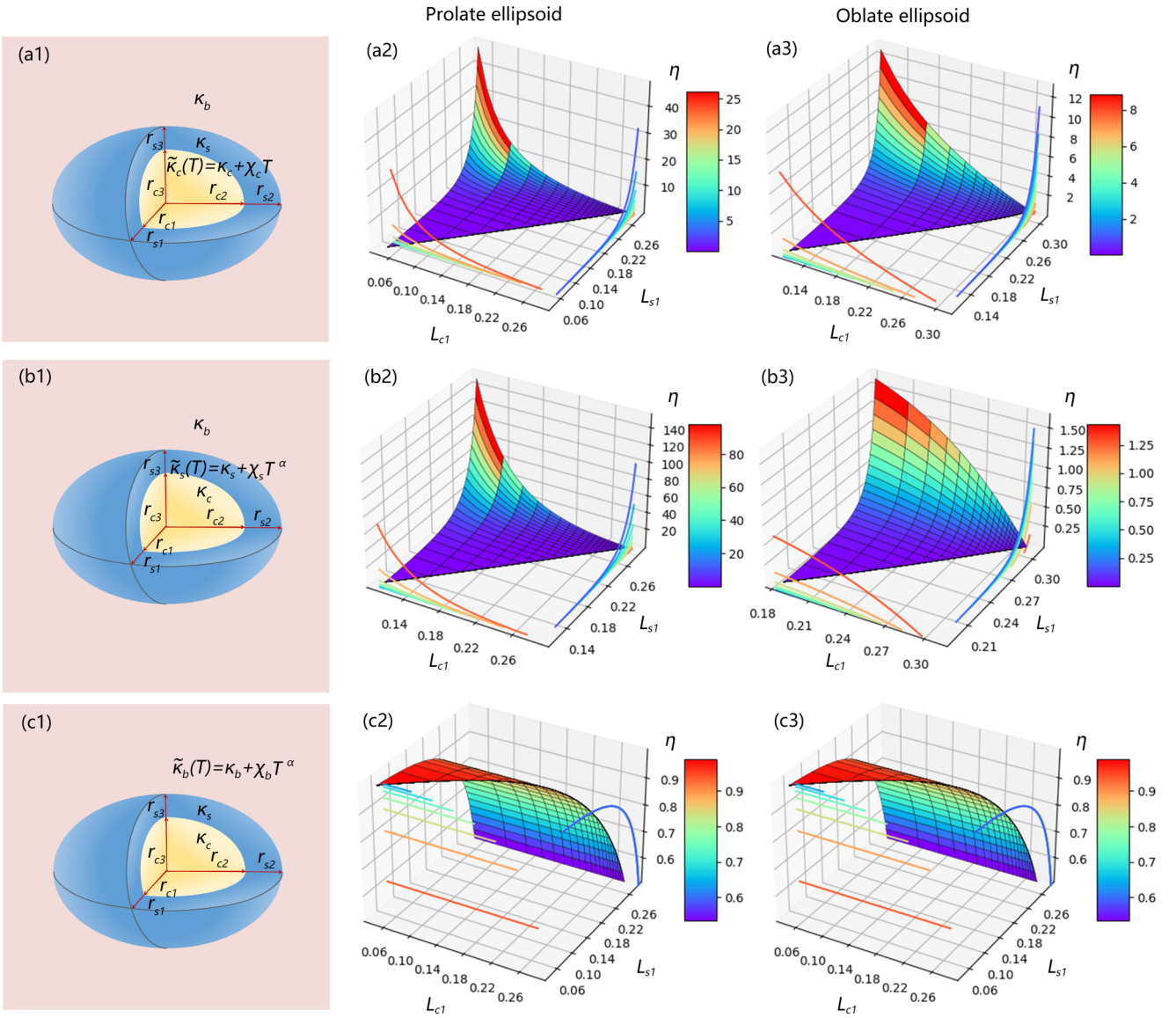

FIG. 4. Three-dimensional schematic diagram of the composite structure with (a1) nonlinear core, (b1) nonlinear shell, or (c1) nonlinear background under the coupling condition. (a2), (a3) [(b2), (b3) or (c2), (c3)] The nonlinear modulation coefficient η of (a1) [(b1) or (c1)] as a function of configuration L_{c1} and L_{s1}. (a2), (b2), (c2) With prolate ellipsoid. (a3), (b3), (c3) With oblate ellipsoid. (a2)–(c3) The color lines in the left (or right) side show η as a function of L_{c1} (or L_{s1}) with constant L_{s1} (or L_{c1}). Parameters: $c^2 = 4.69$, and background size $8\times6\times6$ cm^3 for (a1)–(c3).

III. FINITE-ELEMENT SIMULATIONS FOR VERIFYING THEORETICAL PREDICTIONS

Here, we propose a framework to confirm our theoretical predictions in the two-dimensional case by finite-element simulation (COMSOL Multiphysics). Without loss of generality, we consider a prolate confocal ellipse structure embedded in a finite background. The left and right boundaries are set at 373 K and 273 K, respectively. The upper and lower boundaries are adiabatic. The key point is to obtain the nonlinear modulation coefficient of the structure. For this purpose, we calculate the effective thermal conductivity by $\tilde{\kappa}_{ei}(T) = \langle \boldsymbol{J} \rangle / |\nabla T_0|$, where $\langle \boldsymbol{J} \rangle$ is the overall average heat flux extracted from COMSOL Multiphysics, $|\nabla T_0|$ is equal to the absolute value of the temperature difference between the left and right boundary heat sources. Then, we can derive the nonlinear modulation coefficient by $\eta^{(c)} = (\tilde{\kappa}_{ei}^{(c)}(T) - \kappa_{ei})/\chi_c T^{\alpha}$.

Figure 5 displays the variation trend (the blue dash lines and blue dash-dot lines) of area fraction with shape factor. We can see as the shape factor L_{c1} increases, the area fraction f_1 increases monotonically. And as the shape factor L_{s1} increases, the area fraction f_1 (or f_2) decreases (or increases) monotonically. Then, we compare the theoretical curves (the red solid lines) with the simulation results (the red triangles) in the general case. The left (or right) column represents η as a function of L_{c1} (L_{s1}) with constant L_{s1} (or L_{c1}). When $\eta > 1$, we say that nonlinear enhancement has occurred, namely, $\chi_{ei}^{(c)} > \chi_c$, $\chi_{ei}^{(s)} > \chi_s$ or $\chi_{ei}^{(b)} > \chi_b$. As shown in Fig. 5, the nonlinear modulation coefficient is larger than the dashed black line ($\eta = 1$), which indicates that η

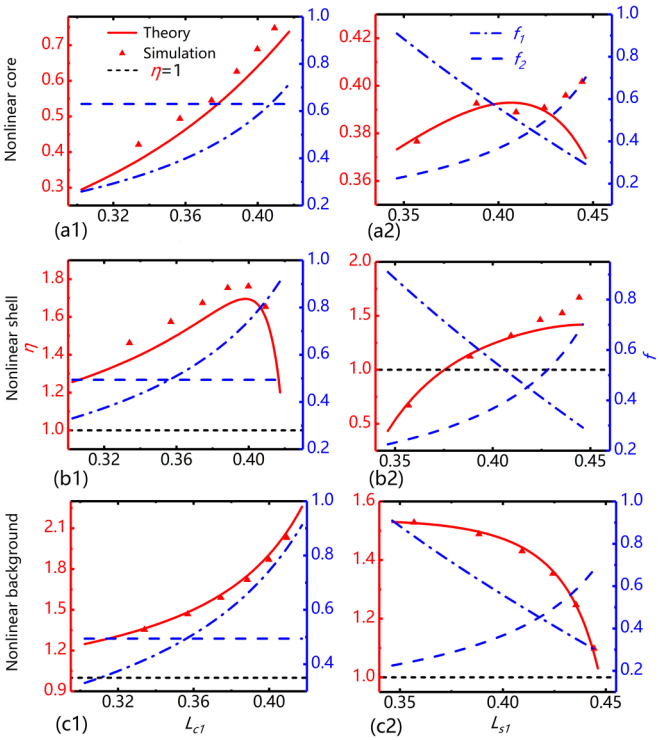

FIG. 5. The nonlinear modulation coefficients η predicted by Eq. (6) (red solid lines) are compared with the two-dimensional simulation results (red triangles). The nonlinear enhancement occurs with η larger than 1 (black dash lines). The variation trends of area fraction f_1 (blue dash-dot lines) and f_2 (blue dash lines) with shape factors are also plotted respectively. (a1)–(a2) With nonlinear core. (b1)–(b2) With nonlinear shell. (c1)–(c2) With nonlinear background. Parameters: (a1), (b1), (c1) $L_{s1} = 0.424$; (a2), (b2), (c2) $L_{c1} = 0.333$; (a1)–(a2) $\tilde{\kappa}_c(T) = 10 + 0.001T$ W m^{-1} K^{-1}, $\kappa_s = 100$ W m^{-1} K^{-1}, and $\kappa_b = 200$ W m^{-1} K^{-1}; (b1)–(b2) $\kappa_c = 100$ W m^{-1} K^{-1}, $\tilde{\kappa}_s(T) = 10 + 0.001T$ W m^{-1} K^{-1}, and $\kappa_b = 200$ W m^{-1} K^{-1}; (c1)–(c2) $\kappa_c = 200$ W m^{-1} K^{-1}, $\kappa_s = 20$ W m^{-1} K^{-1}, and $\kappa_b = 10 + 0.001T$ W m^{-1} K^{-1}; and $c^2 = 4.69$ and background size 8×6 cm^2 for (a1)–(c2).

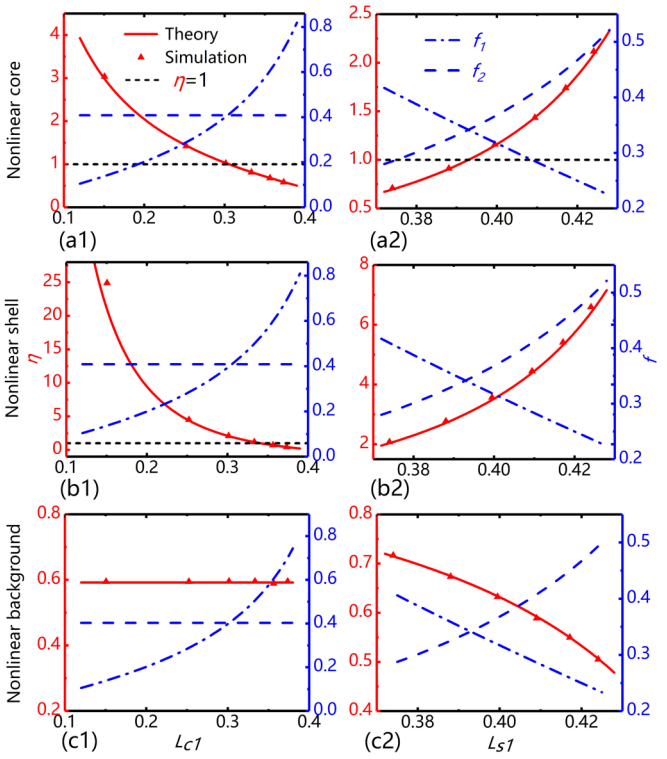

FIG. 6. The nonlinear modulation coefficients η predicted by Eq. (10) (red solid lines) are compared with the two-dimensional simulation results (red triangles). The nonlinear enhancement occurs with η larger than 1 (black dash lines). The variation trends of area fraction f_1 (blue dash-dot lines) and f_2 (blue dash lines) with shape factors are also plotted respectively. (a1)–(a2) With nonlinear core. (b1)–(b2) With nonlinear shell. (c1)–(c2) With nonlinear background. Parameters: (a1), (b1), (c1) $L_{s1} = 0.409$; (a2), (b2), (c2) $L_{c1} = 0.252$; (a1)–(a2) $\tilde{\kappa}_c(T) = 400 + 0.01T$ W m^{-1} K^{-1} and $\kappa_b = 400$ W m^{-1} K^{-1}; (b1)–(b2) $\kappa_c = \kappa_b = 400$ W m^{-1} K^{-1} and $\tilde{\kappa}_s(T) = \kappa_s + 0.004T$ W m^{-1} K^{-1}; (c1)–(c2) $\kappa_c = 400$ W m^{-1} K^{-1} and $\kappa_b = 400 + 0.01T$ W m^{-1} K^{-1}; and $c^2 = 4.69$, background size 8×6 cm^2, and κ_s is determined by Eq. (19) for (a1)–(c2).

can be enhanced in the general case. Similarly, it can be seen from Fig. 6 that η is a function of L_{c1} or L_{s1} in the coupling condition. The simulation results agree well with theoretical predictions, which validates Eqs. (6) and (10). When the appropriate physical parameters are selected, the nonlinear thermal conductivity can be enhanced to one or two orders of magnitude.

In the same way, we take advantage of finite-element simulations (COMSOL Multiphysics) to confirm our theoretical predictions in the three-dimensional case. Without loss of generality, we consider a prolate confocal ellipsoid structure embedded in a finite background. The left and right boundaries are set at 373 K and 273 K, respectively. The upper, lower, front, and back boundaries are adiabatic. To measure the nonlinear modulation coefficient η, we calculate the effective thermal conductivity by $\tilde{\kappa}_{ei}(T) = \langle \boldsymbol{J} \rangle / |\nabla T_0|$. Here, $\langle \boldsymbol{J} \rangle$ is the overall average heat flux obtained from COMSOL Multiphysics, $|\nabla T_0|$ is equal to the absolute value of the temperature difference between the left and right boundary heat sources. Then, we can derive the nonlinear modulation coefficient by $\eta^{(c)} = (\tilde{\kappa}_{ei}^{(c)}(T) - \kappa_{ei})/\chi_c T^{\alpha}$.

The theoretical predictions (the red triangles) in the general case and coupling conditions are respectively displayed in Figs. 7 and 8. The left (or right) column represents η as a function of L_{c1} (L_{s1}) with constant L_{s1} (or L_{c1}). The simulation results (the red triangles) agree well with theoretical predictions (the red solid lines), which validates Eqs. (17) and (20). When the nonlinear modulation coefficient (the red solid lines) is larger than 1 (the black dash lines), we say that the nonlinear enhancement has occurred. As shown in Figs. 7 and 8, we can draw a conclusion that η can be enhanced in the general case and coupling conditions. In addition, the variation trend (the blue dash lines and blue dash-dot lines) between area fraction and shape factors in the three-dimensional case is the same as that in the two-dimensional case, though we can not directly write the relationship between them.

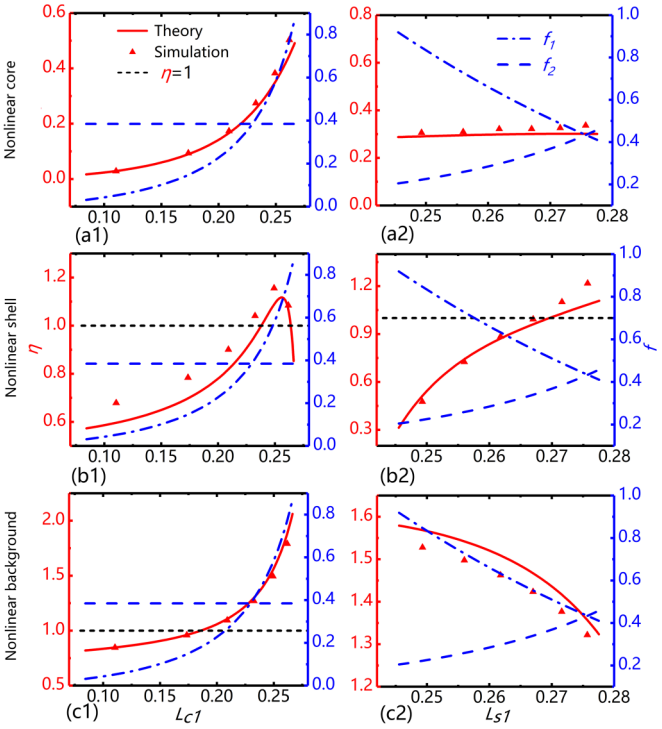

FIG. 7. The nonlinear modulation coefficients η predicted by Eq. (17) (red solid lines) are compared with the three-dimensional simulation results (red triangles). The nonlinear enhancement occurs with η larger than 1 (black dash lines). The variation trends of area fraction f_1 (blue dash-dot lines) and f_2 (blue dash lines) with shape factors are also plotted respectively. (a1)–(a2) With nonlinear core. (b1)–(b2) With nonlinear shell. (c1)–(c2) With nonlinear background. Parameters: (a1), (b1), (c1) $L_{s1} = 0.242$; (a2), (b2), (c2) $L_{c1} = 0.174$; (a1)–(a2) $\tilde{\kappa}_c(T) = 10 + 0.001T$ W m^{-1} K^{-1}, $\kappa_s = 100$ W m^{-1} K^{-1}, and $\kappa_b = 200$ W m^{-1} K^{-1}; (b1)–(b2) $\kappa_c = 100$ W m^{-1} K^{-1}, $\tilde{\kappa}_s(T) = 10 + 0.001T$ W m^{-1} K^{-1}, and $\kappa_b = 200$ W m^{-1} K^{-1}; (c1)–(c2) $\kappa_c = 200$ W m^{-1} K^{-1}, $\kappa_s = 20$ W m^{-1} K^{-1}, and $\kappa_b = 10 + 0.001T$ W m^{-1} K^{-1}; and $c^2 = 4.69$ and background size 8×6 cm^2 for (a1)–(c2).

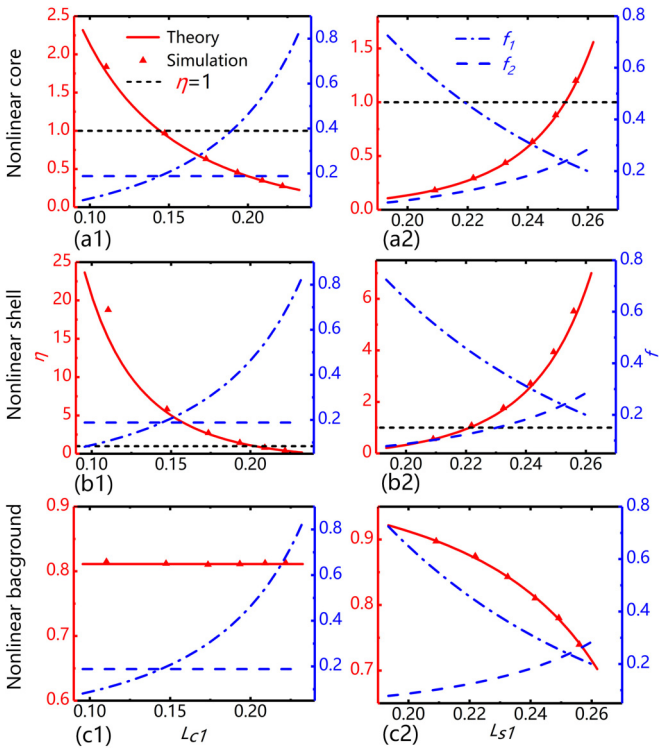

FIG. 8. The nonlinear modulation coefficients η predicted by Eq. (20) (red solid lines) are compared with the three-dimensional simulation results (red triangles). The nonlinear enhancement occurs with η larger than 1 (black dash lines). The variation trends of area fraction f_1 (blue dash-dot lines) and f_2 (blue dash lines) with shape factors are also plotted respectively. (a1)–(a2) With nonlinear core. (b1)–(b2) With nonlinear shell. (c1)–(c2) With nonlinear background. Parameters: (a1), (b1), (c1) $L_{s1} = 0.272$; (a2), (b2), (c2) $L_{c1} = 0.243$; (a1)–(a2) $\tilde{\kappa}_c(T) = 400 + 0.004T$ W m^{-1} K^{-1} and $\kappa_b = 400$ W m^{-1} K^{-1}; (b1)–(b2) $\kappa_c = \kappa_b = 400$ W m^{-1} K^{-1} and $\tilde{\kappa}_s(T) = \kappa_s + 0.004T$ W m^{-1} K^{-1}; (c1)-(c2) $\kappa_c = 400$ W m^{-1} K^{-1} and $\kappa_b = 400 + 0.004T$ W m^{-1} K^{-1}; and $c^2 = 4.69$, background size $8\times6\times6$ cm^3, and κ_s is determined by Eq. (19) for (a1)–(c2).

IV. TWO APPLICATION SCHEMES UNDER THEORETICAL FRAMEWORKS

A. Temperature switching device: Cloaking at high temperature and concentrating at low temperature

By introducing temperature-dependent parameters, an additional degree of control freedom is achieved for manipulating heat flux. Here, we design two kinds of intelligent (switchable) thermal devices based on the proposed theory. We consider the effective nonlinear thermal conductivity due to thermal radiation. According to the Rosseland diffusion approximation, thermal radiation is of T^3 temperature dependence. In a passive and steady process of heat transfer, the total heat flux $\boldsymbol{J}_{\text{total}}$ (consisting of the conductive flux $\boldsymbol{J}_{\text{con}}$ and the radiative flux $\boldsymbol{J}_{\text{rad}}$) is divergency free:

$$\nabla \cdot (\boldsymbol{J}_{\text{con}} + \boldsymbol{J}_{\text{rad}}) = 0. \tag{21}$$

The conductive flux is determined by the Fourier law: $\boldsymbol{J}_{\text{con}} = -\kappa \nabla T$ and the radiative flux is given by the Rosseland diffusion approximation: $\boldsymbol{J}_{\text{rad}} = -\gamma T^3 \nabla T$. Here, $\gamma = 16\tau^{-1} n^2 \sigma / 3$, τ is the Rosseland mean extinction coefficient, n is the relative refractive index, and σ is the Stefan-Boltzmann constant (5.67×10^{-8} W m^{-2} K^{-4}). Then, Eq. (21) can be rewritten as

$$\nabla \cdot [(\kappa + \gamma T^3) \nabla T] = 0. \tag{22}$$

Therefore, we can treat the radiation-conduction process as the heat conduction process with nonlinear thermal conductivity, namely, $\tilde{\kappa}(T) = \kappa + \gamma T^3$. Then, we design intelligent radiation devices, which can achieve thermal concentrating at low temperature [Fig. 9(a)] and thermal cloaking at high temperature [Fig. 9(b)]. The heat conduction dominates when the temperature is low, so the total thermal conductivity only retains the linear term. Since the total thermal conductivity of the core is less than that of the background, the function of thermal concentrator will be realized. The thermal radiation is dominant when the temperature is high, so the total thermal conductivity only

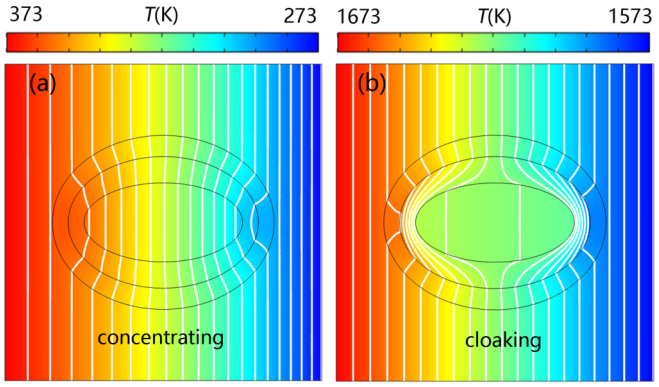

FIG. 9. (a) Thermal cloaking at low temperature. (b) Thermal concentrating at high temperature. Parameters: (a)–(b) $r_{c1} = 2.5$ cm, $r_{c2} = 1.25$ cm, $r_{s1} = 3$ cm, $r_{s2} = 2.08$ cm, $r_t = 3.5$ cm, $r_{t2} = 2.75$ cm, background size 10×10 cm^2, $\tilde{\kappa}_c(T) = 1 + 10^{-1}T^3$ W m^{-1} K^{-1}, $\kappa_s = 50$ W m^{-1} K^{-1}, $\tilde{\kappa}_t(T) = 200 + 5\times10^{-3}T^3$ W m^{-1} K^{-1}, and $\tilde{\kappa}_b(T) = 300 + 1.3\times10^{-3}T^3$ W m^{-1} K^{-1}.

retains the nonlinear term. The core is wrapped by the first shell with a thermal conductivity close to zero, so the heat flux is prevent from entering the core. In addition, the second shell makes the effective thermal conductivity of the multilayer structure equal to that of the background so that the background isotherm is not disturbed, achieving thermal cloaking.

B. Direction switching cloak and concentrator: Open in a specific direction and closed in the opposite direction

Two steady states are necessary for switchable functionalities. A common method in macroscopic system is adopting phase-change materials [35], which are also regarded as nonlinear thermal materials. Here, based on the theory of nonlinearity enhancement, we introduce another asymmetric distribution of thermal conductivity to realize the unidirectional thermal concentrator and thermal cloak. These direction switching devices will be open in a specific direction and closed in the opposite direction.

In Figs. 10(a)–10(c), the device has a linear core and a nonlinear shell. To achieve the effect of switching, we split the shell into two parts [Fig. 10(a)]. The thermal conductivity of the left (or right) part is positively (or negatively) correlated with temperature. Therefore, the effective thermal conductivity of the core-shell structure will be different with two heat fluxes in opposite directions. When the heat flux flows from left to right [Fig. 10(b)], the isotherms inside the device are bent and compressed to the center. Meanwhile, the isotherms outside the device are straight, yielding the phenomenon of thermal concentrator (open state). On the contrary, if the heat flux goes from right to left [Fig. 10(c)], the effective thermal conductivity of the core-shell structure will change greatly. Thus, the isotherms outside the device are disturbed and the device turns to the closed state.

Besides, in Figs. 10(d)–10(f), we consider a split nonlinear core and a linear shell [Fig. 10(d)]. Similarly, the cloak is open

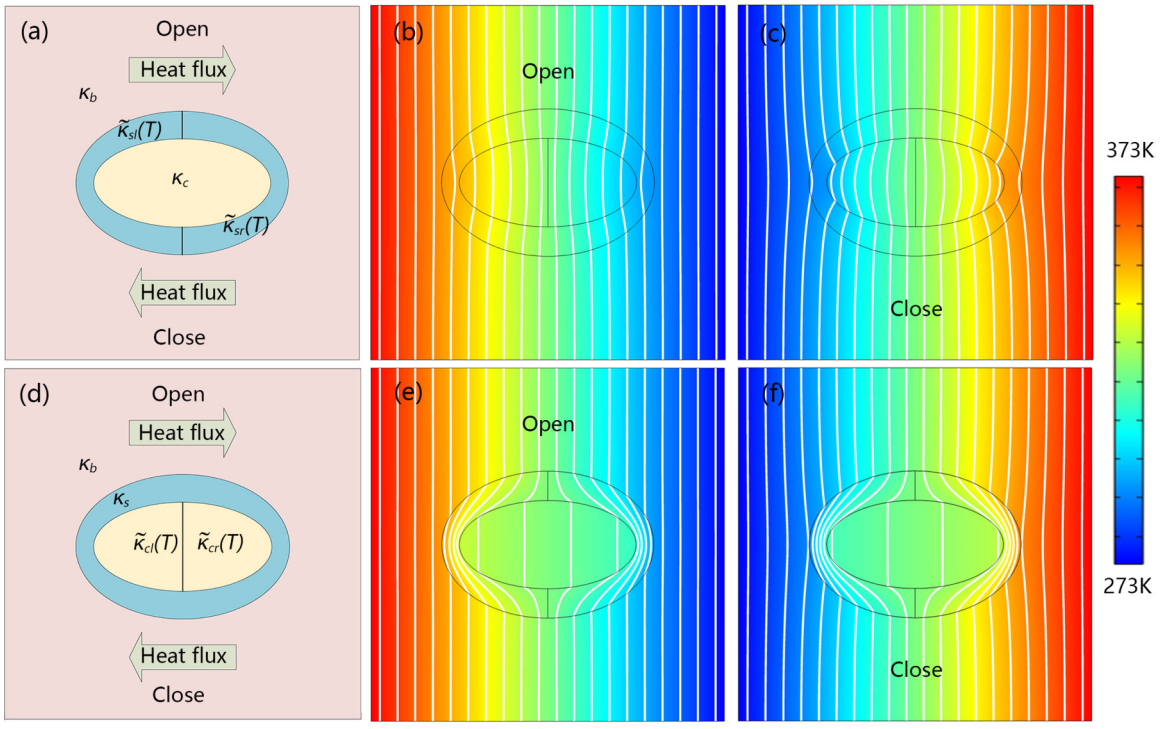

FIG. 10. Direction switching thermal devices. (a) Schematic diagram of thermal concentrator with split nonlinear shell. (b)–(c) The simulation results corresponding to (a). (d) Schematic diagram of thermal cloak with split nonlinear core. (e)–(f) The simulation results corresponding to (d). Parameters: (a)–(c) $\kappa_c = 400$ W m^{-1} K^{-1}, $\tilde{\kappa}_{sl}(T) = 25 + 0.25\times10^{-3}T^3$ W m^{-1} K^{-1}, $\tilde{\kappa}_{sr}(T) = 25 - 0.25T$ W m^{-1} K^{-1}, $\kappa_b = 100$ W m^{-1} K^{-1}; (d)–(f) $\tilde{\kappa}_{cl}(T) = 100 + 3T$ W m^{-1} K^{-1}, $\tilde{\kappa}_{cr}(T) = 100 - 3T$ W m^{-1} K^{-1}, $\kappa_s = 250$ W m^{-1} K^{-1}, $\kappa_b = 200$ W m^{-1} K^{-1}; and $r_{c1} = 2.5$ cm, $r_{c2} = 1.25$ cm, $r_{s1} = 3$ cm, $r_{s2} = 2.08$ cm for (a)–(e).

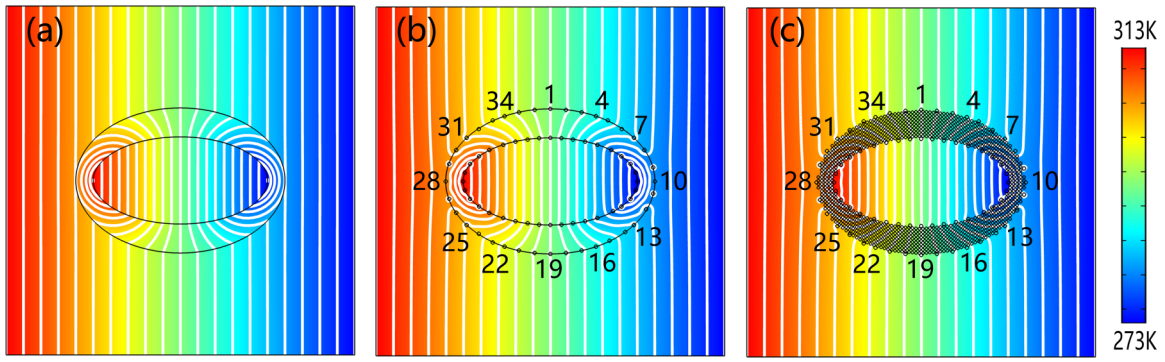

FIG. 11. (a) Aimed simulation result with negative thermal conductivity. (b) and (c) Achieve the same effect as panel (a) with point heat sources whose temperatures are shown in Tables I and II. The shell region is composed of a brass plate (109 W m^{-1} K^{-1}) drilled with 948 air circles with a radius of 0.04 cm, providing a thermal conductivity of 37 W m^{-1} K^{-1} for (c). Other parameters: (a) $\kappa_s = -37$ W m^{-1} K^{-1}; (b) $\kappa_s = 37$ W m^{-1} K^{-1}; and $r_{c1} = 2.5$ cm, $r_{c2} = 1.25$ cm, $r_{s1} = 3$ cm, $r_{s2} = 2.08$ cm, $\kappa_c = \kappa_b = 109$ W m^{-1} K^{-1} for (a)–(c).

for flux flowing from left to right and closed for flux going from right to left.

V. EXPERIMENTAL SUGGESTIONS FOR PROOF-OF-PRINCIPLE VALIDATION

Existing experimental realization for nonlinear thermal metamaterials mainly employs strongly nonlinear materials such as phase-change materials [31,35]. However, their thermal response is speedy and drastic, which may not be applicable for the weak nonlinearity discussed in this work. The apparent negative thermal conductivities [49,50] proposed above are applied in the shell due to the coupling condition, which cannot occur spontaneously in experiments. By considering the uniqueness theorem, we keep the boundary conditions in Fig. 11(b) consistent with those in Fig. 11(a). The aimed temperature distributions with negative thermal conductivity would be achieved without violating the second law of thermal dynamics. To solve this problem, a series of point heat sources are added at the inner and outer boundaries of the shell [Figs. 11(b) and 11(c)], and the concrete temperatures are given in Tables I and II. We can adjust the temperature of a series of thermostatic water baths by heating and cooling rods. Then, we connect the inner (or outer) boundary with these thermostatic water baths by heat pipes for realizing point heat sources. The thermal conductivity of the shell in Fig. 11(b) is the opposite of that in Fig. 11(a) and the point heat sources are added in Fig. 11(b). Nevertheless, the temperature distributions in Figs. 11(b) and 11(a) are almost the same, so we confirm that adding external heat sources can realize a apparent negative thermal conductivity. Moreover, we design a feasible scheme as an experimental suggestion [Fig. 11(c)]. We put the left and right edges of a brass plate (109 W m^{-1}K^{-1}) fabricated by laser cutting into hot (313 K) and cold (273 K) sinks. To achieve the thermal conductivity of the shell region in Fig. 11(b), 948 air circles with a radius of 0.04 cm are drilled on the brass, providing a thermal conductivity of 37 W m^{-1}K^{-1} (calculated by Eq. (11) in Ref. [58]). By comparing the temperature profiles in Figs. 11(a)–11(c), we can draw a conclusion that the structure in Fig. 11(c) can realize the effect of Fig. 11(a) in experiments.

VI. DISCUSSION AND CONCLUSION

In this work, we have discussed the nonlinearity enhancement effects in geometrically anisotropic composites. By introducing shape factors, we demonstrate a unified theory for treating anisotropic medium. The derived results apply to the previous isotropic cases [41] if the shape factor is taken as an isotropic value. To vividly understand the idea of nonlinearity enhancement, we propose a group of coupling conditions, which can realize thermal transparency effects [54]. We

TABLE I. Temperatures of point heat sources at the inner boundary of the shell in Figs. 11(b) and 11(c).

Source	Temp. (K)	Source	Temp. (K)	Source	Temp. (K)	Source	Temp. (K)
1	293.00	10	273.08	19	293.00	28	312.92
2	290.45	11	273.48	20	295.55	29	312.52
3	287.82	12	274.67	21	298.18	30	311.33
4	285.03	13	276.75	22	300.97	31	309.25
5	282.24	14	279.06	23	303.76	32	306.94
6	279.06	15	282.24	24	306.94	33	303.76
7	276.75	16	285.03	25	309.25	34	300.97
8	274.67	17	287.82	26	311.33	35	298.18
9	273.48	18	290.45	27	312.52	36	295.55

TABLE II. Temperatures of point heat sources at the outer boundary of the shell in Figs. 11(b) and 11(c).

Source	Temp. (K)	Source	Temp. (K)	Source	Temp. (K)	Source	Temp. (K)
1	293.00	10	280.95	19	293.00	28	305.05
2	291.19	11	281.16	20	294.81	29	304.84
3	289.39	12	282.16	21	296.61	30	303.84
4	287.74	13	283.36	22	298.26	31	302.64
5	286.37	14	284.77	23	299.62	32	301.23
6	284.77	15	286.37	24	301.23	33	299.62
7	283.36	16	287.74	25	302.64	34	298.26
8	282.16	17	289.39	26	303.84	35	296.61
9	281.16	18	291.19	27	304.84	36	294.81

further point out coupling conditions require negative thermal conductivities, which can be effectively achieved by external energy or thermoelectric materials in real physical systems [10,39,59,60]. It is noted that the coupling conditions may greatly increase the nonlinearity enhancement. Spontaneous evolution inside systems can only induce weak nonlinearity enhancement, which may hardly be observed or utilized. On the other hand, anisotropy in architecture induces an additional degree of freedom beyond isotropic composites, benefiting more obvious enhancement effects. This result may promote the application of nonlinearity enhancement in various fields such as wavelike heat transport or thermal harmonic generation.

To sum up, we investigate the nonlinear enhancement effect of a core-shell structure embedded in a finite background, which may have potential applications in thermal management. We calculate the nonlinear modulation coefficient η in the general case and execute a reparameterization process for characterizing it by independent geometric parameters. Then, we consider the nonlinear enhancement effect in the coupling condition, which is convenient for us to discuss the relationship between η and the relevant parameters. Finite-element simulations verify these theoretical results. We also provide a feasible experimental suggestion. In addition, we design two types of intelligent thermal devices in proof of principle for promoting practical applications. It is promising to extend the related mechanisms of the basic model in this work to other anisotropic models or even multifield coupling systems.

ACKNOWLEDGMENTS

We acknowledge financial support from the National Natural Science Foundation of China (Grants No. 11725521, No. 12035004, and No. 12147169), and the Science and Technology Commission of Shanghai Municipality (Grant No. 20JC1414700).

[1] C. Z. Fan, Y. Gao, and J. P. Huang, Shaped graded materials with an apparent negative thermal conductivity, Appl. Phys. Lett. **92**, 251907 (2008).
[2] T. Y. Chen, C. N. Weng, and J. S. Chen, Cloak for curvilinearly anisotropic media in conduction, Appl. Phys. Lett. **93**, 114103 (2008).
[3] M. Maldovan, Sound and heat revolutions in phononics, Nature (London) **503**, 209 (2013).
[4] S. Yang, J. Wang, G. L. Dai, F. B. Yang, and J. P. Huang, Controlling macroscopic heat transfer with thermal metamaterials: Theory, experiment and application, Phys. Rep. **908**, 1 (2021).
[5] Y. Li, W. Li, T. C. Han, X. Zheng, J. X. Li, B. W. Li, S. H. Fan, and C.-W. Qiu, Transforming heat transfer with thermal metamaterials and devices, Nat. Rev. Mater. **6**, 488 (2021).
[6] W. Sha, M. Xiao, J. H. Zhang, X. C. Ren, Z. Zhu, Y. Zhang, G. Q. Xu, H. G. Li, X. L. Liu, X. Chen, L. Gao, C.-W. Qiu, and R. Hu, Robustly printable freeform thermal metamaterials, Nat. Commun. **12**, 7228 (2021).
[7] W. Sha, R. Hu, M. Xiao, S. Chu, Z. Zhu, C.-W. Qiu, and L. Gao, Topology-optimized thermal metamaterials traversing full-parameter anisotropic space, npj Comput. Mater. **8**, 179 (2022).
[8] R. Hu, S. Y. Huang, M. Wang, X. B. Luo, J. Shiomi, and C.-W. Qiu, Encrypted Thermal Printing with regionalization transformation, Adv. Mater. **31**, 1807849 (2019).
[9] M. Wegener, Metamaterials beyond optics, Science **342**, 939 (2013).
[10] D. M. Nguyen, H. Y. Xu, Y. M. Zhang, and B. L. Zhang, Active thermal cloak, Appl. Phys. Lett. **107**, 121901 (2015).
[11] F. Y. Yang, F. S. Hung, W. S. Yeung, and Y. J. Yang, Optimization Method for Practical Design of Planar Arbitrary-Geometry Thermal Cloaks Using Natural Materials, Phys. Rev. Appl. **15**, 024010 (2021).
[12] L. J. Xu, G. L. Dai, G. Wang, and J. P. Huang, Geometric phase and bilayer cloak in macroscopic particle-diffusion systems, Phys. Rev. E **102**, 032140 (2020).
[13] T. Sun, X. H. Wang, X. Y. Yang, T. Meng, R. Y. He, and Y. X. Wang, Design of thermal cloak and concentrator with interconnected structure, Int. J. Heat Mass Transf. **187**, 122568 (2022).
[14] S. Guenneau, C. Amra, and D. Veynante, Transformation thermodynamics: Cloaking and concentrating heat flux, Opt. Express **20**, 8207 (2012).
[15] M. Moccia, G. Castaldi, S. Savo, Y. Sato, and V. Galdi, Independent Manipulation of Heat and Electrical Current via Bifunctional Metamaterials, Phys. Rev. X **4**, 021025 (2014).
[16] F. Chen and D. Y. Lei, Experimental realization of extreme heat flux concentration with easy-to-make thermal metamaterials, Sci. Rep. **5**, 11552 (2015).
[17] G. Q. Xu, X. Zhou, and Z. J. Liu, Converging heat transfer in completely arbitrary profiles with unconventional thermal concentrator, Int. Commun. Heat Mass Transf. **108**, 104337 (2019).
[18] L. J. Xu, S. Yang, and J. P. Huang, Thermal theory for heterogeneously architected structure: Fundamentals and application, Phys. Rev. E **98**, 052128 (2018).
[19] G. Fujii and Y. Akimoto, Cloaking a concentrator in thermal conduction via topology optimization, Int. J. Heat Mass Transf. **159**, 120082 (2020).
[20] Q. X. Ji, X. Y. Chen, J. Liang, V. Laude, S. Guenneau, G. D. Fang, and M. Kadic, Designing thermal energy harvesting devices with natural materials through optimized microstructures, Int. J. Heat Mass Transf. **169**, 120948 (2021).
[21] F. B. Yang, B. Y. Tian, L. J. Xu, and J. P. Huang, Experimental Demonstration of Thermal Chameleonlike Rotators with Transformation-Invariant Metamaterials, Phys. Rev. Appl. **14**, 054024 (2020).
[22] S. Guenneau and C. Amra, Anisotropic conductivity rotates heat fluxes in transient regimes, Opt. Express **21**, 6578 (2013).
[23] R. Hu, W. Xi, Y. D. Liu, K. C. Tang, J. L. Song, X. B. Luo, J. Q. Wu, and C.-W. Qiu, Thermal camouflaging metamaterials, Mater. Today **45**, 120 (2021).
[24] R. Hu, S. L. Zhou, Y. Li, D. Y. Lei, X. B. Luo, and C.-W. Qiu, Illusion thermotics, Adv. Mater. **30**, 1707237 (2018).

[25] C. J. Glassbrenner and G. A. Slack, Thermal conductivity of silicon and germanium from 3°K to the melting point, Phys. Rev. **134**, A1058 (1964).
[26] R. C. Zeller and R. O. Pohl, Thermal conductivity and specific heat of noncrystalline solids, Phys. Rev. B **4**, 2029 (1971).
[27] N. Bloembergen, *Nonlinear Optics* (Benjamin, New York, 1964).
[28] J. P. Huang and K. W. Yu, Enhanced nonlinear optical responses of materials: Composite effects, Phys. Rep. **431**, 87 (2006).
[29] G. L. Dai, Designing nonlinear thermal devices and metamaterials under the Fourier law: A route to nonlinear thermotics, Front. Phys. **16**, 53301 (2021).
[30] Y. Li, X. Y. Shen, Z. H. Wu, J. Y. Huang, Y. X. Chen, Y. S. Ni, and J. P. Huang, Temperature-Dependent Transformation Thermotics: From Switchable Thermal Cloaks to Macroscopic Thermal Diodes, Phys. Rev. Lett. **115**, 195503 (2015).
[31] X. Y. Shen, Y. Li, C. R. Jiang, and J. P. Huang, Temperature Trapping: Energy-Free Maintenance of Constant Temperatures as Ambient Temperature Gradients Change, Phys. Rev. Lett. **117**, 055501 (2016).
[32] T. J. Alexander, High-heat-flux rectification due to a localized thermal diode, Phys. Rev. E **101**, 062122 (2020).
[33] W. X. Zhao, Z. Zhu, Y. W. Fan, W. Xi, R. Hu, and X. B. Luo, Temporally-adjustable radiative thermal diode based on metal-insulator phase change, Int. J. Heat Mass Transf. **185**, 122443 (2022).
[34] M. Lei, J. Wang, G. L. Dai, P. Tan, and J. P. Huang, Temperature-dependent transformation multiphysics and ambient-adaptive multiphysical metamaterials, Europhys. Lett. **135**, 54003 (2021).
[35] X. Y. Shen, Y. Li, C. R. Jiang, Y. S. Ni, and J. P. Huang, Thermal cloak-concentrator, Appl. Phys. Lett. **109**, 031907 (2016).
[36] M. Farhat, S. Guenneau, P. Y. Chen, A. Alù, and K. N. Salama, Scattering Cancellation-Based Cloaking for the Maxwell-Cattaneo Heat Waves, Phys. Rev. Appl. **11**, 044089 (2019).
[37] L. J. Xu and J. P. Huang, Thermal convection-diffusion crystal for prohibition and modulation of wave-like temperature profiles, Appl. Phys. Lett. **117**, 011905 (2020).
[38] L. J. Xu and J. P. Huang, Controlling thermal waves with transformation complex thermotics, Int. J. Heat Mass Transf. **159**, 120133 (2020).
[39] L. J. Xu and J. P. Huang, Active thermal wave cloak, Chin. Phys. Lett. **37**, 120501 (2020).
[40] C. Su, L. J. Xu, and J. P. Huang, Nonlinear thermal conductivities of core-shell metamaterials: Rigorous theory and intelligent application, Europhys. Lett. **130**, 34001 (2020).
[41] S. Yang, L. J. Xu, and J. P. Huang, Metathermotics: Nonlinear thermal responses of core-shell metamaterials, Phys. Rev. E **99**, 042144 (2019).
[42] G. L. Dai and J. P. Huang, Nonlinear thermal conductivity of periodic composites, Int. J. Heat Mass Transf. **147**, 118917 (2020).
[43] J. Wang and G. L. Dai, Configuration-induced directional nonlinearity enhancement in composite thermal media, Front. Phys. **10**, 924890 (2022).
[44] T. C. Han, P. Yang, Ying Li, D. Y. Lei, B. W. Li, K. Hippalgaonkar, and C.-W. Qiu, Full-parameter omnidirectional thermal metadevices of anisotropic geometry, Adv. Mater. **30**, 1804019 (2018).
[45] B. Y. Tian, J. Wang, G. L. Dai, X. P. Ouyang, and J. P. Huang, Thermal metadevices with geometrically anisotropic heterogeneous composites, Int. J. Heat Mass Transf. **174**, 121312 (2021).
[46] S. Yang, L. J. Xu, and J. P. Huang, Intelligence thermotics: Correlated self-fixing behavior of thermal metamaterials, Europhys. Lett. **126**, 54001 (2019).
[47] L. J. Xu, S. Yang, and J. P. Huang, Designing the effective thermal conductivity of materials of core-shell structure: Theory and simulation, Phys. Rev. E **99**, 022107 (2019).
[48] S. Yang, L. J. Xu, and J. P. Huang, Two exact schemes to realize thermal chameleonlike metashells, Europhys. Lett. **128**, 34002 (2019).
[49] P. F. Zhuang, L. J. Xu, P. Tan, X. P. Ouyang, and J. P. Huang, Breaking efficiency limit of thermal concentrators by conductivity couplings, Sci. China Phys. Mech. Astron. **65**, 117007 (2022).
[50] L. J. Xu and J. P. Huang, Negative thermal transport in conduction and advection, Chin. Phys. Lett. **37**, 080502 (2020).
[51] R. Hu, S. Y. Huang, M. Wang, L. L. Zhou, X. Y. Peng, and X. B. Luo, Binary Thermal Encoding by Energy Shielding and Harvesting Units, Phys. Rev. Appl. **10**, 054032 (2018).
[52] L. J. Xu, G. Q. Xu, J. P. Huang, and C.-W. Qiu, Diffusive Fizeau Drag in Spatiotemporal Thermal Metamaterials, Phys. Rev. Lett. **128**, 145901 (2022).
[53] Z. R. Zhang and J. P. Huang, Transformation plasma physics, Chin. Phys. Lett. **39**, 075201 (2022).
[54] L. J. Xu and J. P. Huang, Metamaterials for Manipulating Thermal Radiation: Transparency, Cloak, and Expander, Phys. Rev. Appl. **12**, 044048 (2019).
[55] N. A. Nicorovici and R. C. McPhedran, Optical and dielectric properties of partially resonant composites, Phys. Rev. B **49**, 8479 (1994).
[56] O. Levy, Nonlinear properties of partially resonant composites, J. Appl. Phys. **77**, 1696 (1995).
[57] C. Dames, Solid-state thermal rectification with existing bulk materials, J. Heat Transf. **131**, 061301 (2009).
[58] S. Yang, L. J. Xu, R. Z. Wang, and J. P. Huang, Full control of heat transfer in single-particle structural materials, Appl. Phys. Lett. **111**, 121908 (2017).
[59] L. J. Xu, S. Yang, and J. P. Huang, Dipole-assisted thermotics: Experimental demonstration of dipole-driven thermal invisibility, Phys. Rev. E **100**, 062108 (2019).
[60] L. J. Xu, X. T. Zhao, Y. P. Zhang, and J. P. Huang, Tailoring dipole effects for achieving thermal and electrical invisibility simultaneously, Eur. Phys. J. B **93**, 101 (2020).